

Article

Evaluation of Stray Light Correction for GOCI Remote Sensing Reflectance Using *in Situ* Measurements

Wonkook Kim, Jeong-Eon Moon, Jae-Hyun Ahn and Young-Je Park *

Korea Ocean Satellite Center, Korea Institute of Ocean Science and Technology, 787 Haean-ro, Ansan-si, Gyeonggi-do 15627, Korea; wkkim@kiost.ac (W.K.); jemoon@kiost.ac (J.-E.M.); brtnt@kiost.ac (J.-H.A.)

* Correspondence: youngjepark@kiost.ac; Tel.: +82-31-400-7772

Academic Editors: Xiaofeng Li and Prasad S. Thenkabail

Received: 18 February 2016; Accepted: 28 April 2016; Published: 4 May 2016

Abstract: The Geostationary Ocean Color Imager (GOCI) is the world's first ocean color sensor in geostationary orbit. Although the GOCI has shown excellent radiometric performance with little long-term radiometric degradation and a high signal-to-noise ratio, there are radiometric artefacts in GOCI Level 1 products caused by stray light detected within the GOCI optics. To correct the radiometric bias, we developed an image-based correction algorithm called the correction of the interslot discrepancy using the minimum noise fraction transform (CIDUM) in a previous study and evaluated its performance with respect to the physical radiometric quantity stored in Level 1 products, *i.e.*, top-of-atmosphere radiance. This study evaluated the performance of the CIDUM algorithm in terms of remote sensing reflectance, which is one of the most important products in ocean color remote sensing. The resultant CIDUM-corrected remote sensing reflectance products were validated using both relative (within the image) and absolute references (*in situ* measurements). Image validation showed that CIDUM corrected the bias in remote sensing reflectance (up to 20%) and reduced the bias to $\leq 5\%$ in the tested image. *In situ* validation showed that relative uncertainty was reduced by around 10% within the visible bands and the correlation between the *in situ* and GOCI radiometric data was enhanced.

Keywords: GOCI; ocean color; stray light; CIDUM; remote sensing reflectance; atmospheric correction; validation; *in situ* measurements

1. Introduction

The Geostationary Ocean Color Imager (GOCI) was launched in June 2010 and has produced regional-scale ocean color data over areas of East Asia around the Korean Peninsula [1,2]. GOCI acquires images of the target area (2500 × 2500 km area; centered at 36°N, 130°E) through the “step-and-stare” method, where the entire target area is subdivided into 16 (4 × 4) areas, each of which is sequentially covered by a single 2-dimensional CMOS detector [3]. In the sequential acquisition, the area or portion covered by the single acquisition is referred to as a “slot”. Radiometric data for each slot is stored in a Level 1A (L1A) file and the images for all the slots are later combined into a mosaicked image (Level 1B (L1B) data) of the entire target area through re-projection to the GOCI orthogonal map projection.

Ideally, boundary areas between adjacent slots should not exhibit any systematic radiometric discontinuity other than that created by natural variability. This is induced mainly through differences in image acquisition times and it usually does not exceed 3% in the normalized top-of-atmosphere (TOA) radiance [4]. However, previous experiments [4] have shown that strong interslot radiometric discrepancy (ISRD) of up to 20% exists in the normalized TOA radiance in the red (680 nm) and near-infrared (NIR) (865 nm) bands for slot pairs with N–S alignment. The requirement of radiometric

uncertainty for the visible to NIR bands of earth observing satellites is usually ~2% and there are stricter requirements for ocean color sensors. Thus, an ISRD of 20% is an extraordinarily large bias that could jeopardize the atmospheric correction procedure. Moreover, radiometric bias causes significant problems in the algorithms that use information from the spectral bands that are affected by ISRD (e.g., the fluorescence line height method for estimating chlorophyll concentration).

One of the major artificial sources of ISRD is stray light that occurs within the sensor optics. A ray-tracing simulation [5] demonstrated that stray light from various optical paths within the GOCI sensor optics could generate radiometric inflation, particularly for the lower parts of each slot. We refer to the radiometric anomaly caused by stray light within the sensor optics as stray-light-driven radiometric inflation (SLRI). Naturally, the existence of SLRI in one slot creates ISRD between adjacent slots. The intensity of SLRI depends on both the location and the reflectivity of bright targets near the target area (mostly from northern parts of the target point), making the spatiotemporal pattern of SLRI variability dependent on the surrounding environment.

To mitigate the degree of SLRI in GOCI L1B images, we proposed an image-based correction algorithm called the correction of inter-slot radiometric discrepancy using the minimum noise fraction transform (CIDUM) [4]. The CIDUM algorithm comprises three steps. (1) First, the spatial distribution of SLRI is identified in individual slots using the minimum noise fraction (MNF) transform [6]; (2) Then, the extracted pattern is scaled to the actual SLRI using the pixels in the slot overlaps; (3) Finally, the estimated SLRI is subtracted from the original L1A image. CIDUM recovers the discontinuity in the slot boundaries in L1B data (TOA radiance) successfully, reducing the large SLRI that can reach up to 20% to less than 3% in all the slot boundaries of the tested GOCI data sets [4].

In this study, we performed further validation on the CIDUM algorithm, focusing particularly on the quality of remote sensing reflectance (R_{rs}) that is derived from the atmospheric correction process. Remote sensing reflectance is an important product in ocean color remote sensing because it plays a critical role in the estimation of the concentrations of optically active water constituents such as chlorophyll pigment concentration, suspended sediment concentrations, and dissolved organic matter. The impact of the CIDUM correction on R_{rs} data is not as straightforward as in TOA radiance data. The atmospheric correction process is a nonlinear process that involves an iterative aerosol-estimation procedure, in which a positive bias in TOA radiance does not necessarily induce a positive bias in remote sensing reflectance. Furthermore, the relative portion of SLRI is greater in the Rayleigh-corrected radiance than in TOA radiance, making the aerosol-estimation process based on band ratios more sensitive to SLRI.

Two approaches were adopted to validate the results in R_{rs} . In the first approach, improvements in R_{rs} after the application of CIDUM were quantified at the slot boundary by comparing the R_{rs} of nearby pixels from different slots. A ray-tracing simulation [5] has shown that the upper part of a slot is affected little by SLRI, allowing those boundary areas beneath the slot boundary to be used as the reference spectrum for the assessment of the results of the correction in the upper slot. Although there is a difference between the acquisition times of the two slots, comparison of both the corrected and the uncorrected data with the reference data can provide insight into the correction quality. The second approach used an absolute validation based on independent *in situ* radiometric measurements. Whereas the first approach (hereafter, referred to as “boundary analysis”) evaluated the relative performance of the correction within the restricted area (feasible only near the slot boundary), the second approach evaluated the absolute performance of the correction, including those areas far from the slot boundary.

2. Materials and Methods

2.1. CIDUM Algorithm with Minor Modification

For the validation in this study, a slight modification was applied to the previously proposed CIDUM algorithm [4] to improve the removal of SLRI from the data. Previously, in the original

proposal, the SLRI pattern extracted from the MNF transform was scaled based on the radiometric differences of the slot overlaps after normalization to the sun elevation angle, *i.e.*, the normalized TOA radiance. However, the sun elevation angle differs for the different slots causing variation in the level of Rayleigh scattering, which increases the uncertainty in the comparison of the TOA radiances in the slot overlaps. In the modified CIDUM, pixels in the slot overlaps were compared in terms of Rayleigh-corrected reflectance rather than normalized TOA radiance.

Here, we provide a brief description of the modified CIDUM algorithm. CIDUM utilizes the MNF transform for the extraction of the SLRI pattern from individual L1A images. The MNF transform is efficient in detecting image artefacts that have strong spatial autocorrelation. For example, the smile effect in Hyperion data, which causes a gradual alteration of the measured radiance in marginal areas of images with a wide angle of view was identified and corrected using the MNF transform [7]. Formulation of the MNF transform was presented in Appendix.

The SLRI patterns extracted from the L1A images are calibrated against the adjacent slots in such a way that the mean statistics of the pixels in the overlapped region are equalized. Specifically, for a pair of slots, the mean Rayleigh-corrected reflectances are supposed equal if there is no SLRI effect, *i.e.*:

$$\rho_{rc}^{(1)} = \rho_{rc}^{(2)} \quad (1)$$

where $\rho_{rc}^{(i)}$ denotes the Rayleigh-corrected reflectance in the i -th slot. The value of $\rho_{rc}^{(i)}$ is calculated from the TOA radiance ($L_{TOA}^{(i)}$) as follows:

$$\rho_{rc}^{(i)} = \rho_{TOA}^{(i)} - \rho_r^{(i)} \quad (2)$$

$$= \frac{\pi L_{TOA}^{(i)}}{\cos\theta_s^{(i)} F_0} - \rho_r^{(i)} \quad (3)$$

where $\rho_{TOA}^{(i)}$ is the TOA reflectance, $\theta_s^{(i)}$ is the solar zenith angle, and $\rho_r^{(i)}$ is the Rayleigh reflectance computed using the 6S code [8]. The unbiased TOA radiance ($L_{TOA}^{(i)}$) is computed by subtracting the SLRI radiance ($L_{SLRI}^{(i)}$) from the observed at-sensor radiance ($L_{obs}^{(i)}$) as

$$L_{TOA}^{(i)} = L_{obs}^{(i)} - L_{SLRI}^{(i)} \quad (4)$$

If we define $k^{(i)}$ as

$$k^{(i)} = \frac{\pi}{\cos\theta_s^{(i)} F_0} \quad (5)$$

where F_0 is the solar irradiance, then Equation (1) can be formulated in terms of the known variables ($L_{obs}^{(i)}$, $k^{(i)}$, and $\rho_r^{(i)}$) and the unknown variables ($L_{SLRI}^{(i)}$) as:

$$k^{(1)} \left(L_{obs}^{(1)} - L_{SLRI}^{(1)} \right) - \rho_r^{(1)} = k^{(2)} \left(L_{obs}^{(2)} - L_{SLRI}^{(2)} \right) - \rho_r^{(2)} \quad (6)$$

$$\left[k^{(1)} L_{obs}^{(1)} - \rho_r^{(1)} \right] - \left[k^{(2)} L_{obs}^{(2)} - \rho_r^{(2)} \right] = k^{(1)} L_{SLRI}^{(1)} - k^{(2)} L_{SLRI}^{(2)} \quad (7)$$

The SLRI radiance ($L_{SLRI}^{(i)}$) is computed from the MNF transform after applying the slot-dependent calibration factor $\alpha^{(i)}$:

$$L_{SLRI}^{(i)} = \alpha^{(i)} X_{MNF}^{(i)} \quad (8)$$

where $X_{MNF}^{(i)}$ is the SLRI signal image extracted from the MNF transform. Now, constructing the equations for all 24 slot pairs generates the linear system that has 16 unknowns (calibration factors for 16 slots) and 24 constraints. Solving the linear system provides an optimal set of calibration factors that minimizes the overall ISRD between all the slot pairs.

2.2. Study Area and Field Measurements

For an independent evaluation of the algorithm, above-water radiometric measurements were acquired off the west coast of Korea using the ASD[®] and TriOS[®] hyperspectral radiometers. After a quality control process that screened the *in situ* measurements for poor-quality data [9], 26 match-up pairs between the *in situ* and the GOCI R_{rs} were identified in the GOCI data over three days (31 July 2012, 16 October 2012, and 23 October 2013), which are dates that had strong SLRI in the corresponding L1B images. Since GOCI images were taken every hour, the maximum time difference between *in situ* measurements and the corresponding GOCI data is 30 min if the *in situ* data were collected between 00:16 UTC and 07:46 UTC. This study used the GOCI Data Processing System (GDPS) atmospheric correction process (version 1.31) [10].

The locations of the 26 measurement stations are displayed in Figure 1 with the background image of L_{TOA} (680) acquired on 31 July 2012 (UTC 02). This area has large spatiotemporal variability in R_{rs} , which is dominated by the variation in suspended sediment concentration. Resuspension from tidal movement in the shallow water and the existence of a mud belt (Heuksan mud belt) in the offshore area cause high concentrations of suspended sediment of 10–100 g/m³. The acquisition times and the geographic coordinates of the *in situ* data are presented in Table 1 for the 26 stations used in the validation.

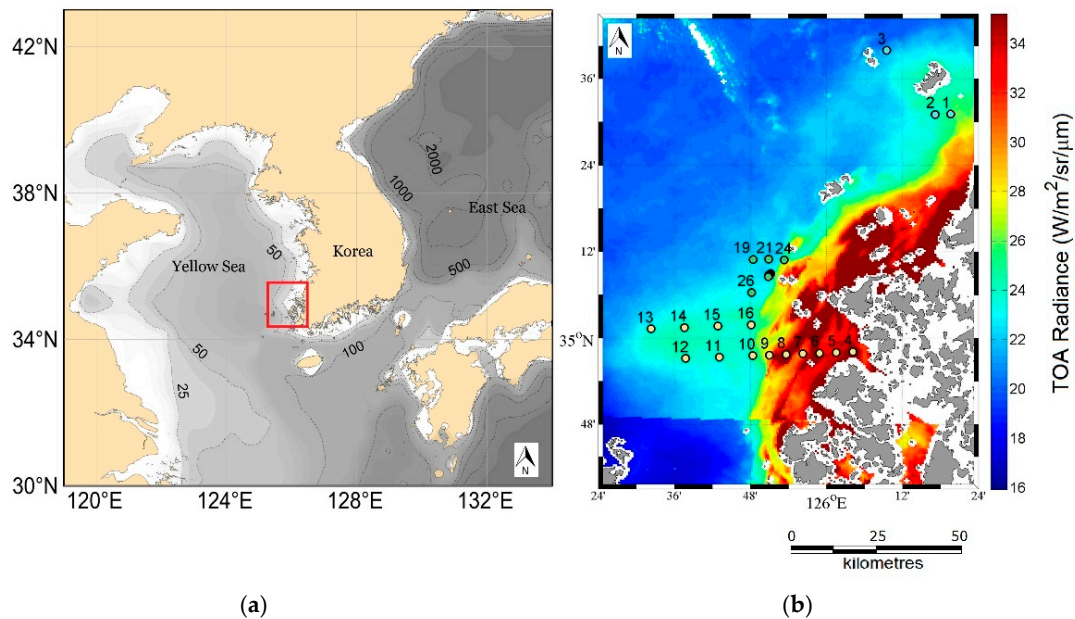


Figure 1. Locations of the study area (a) and the *in situ* measurement sites (b) in the SW coast of Korea are presented. For the station map (b), GOCI image of TOA radiance in the 680-nm band is used as background.

Table 1. Times and locations of the 26 *in situ* radiometric measurements used for this study. Time is in Coordinated Universal Time (UTC).

ID	Year	Month	Day	Latitude	Longitude	Hour	Minute
1	2012	07	31	35.5179	126.3264	02	04
2				35.5178	126.2855	02	23
3				35.6653	126.1580	05	10
4	2012	10	16	34.9686	126.0695	00	10
5				34.9671	126.0255	00	28
6				34.9656	125.9816	00	47
7				34.9642	125.9377	01	04
8				34.9626	125.8938	01	24
9				34.9611	125.8498	01	40

Table 1. Cont.

ID	Year	Month	Day	Latitude	Longitude	Hour	Minute
10				34.9596	125.8059	02	02
11				34.9564	125.7180	02	40
12				34.9533	125.6302	03	02
13				35.0219	125.5384	04	27
14				35.0251	125.6263	04	54
15				35.0283	125.7143	05	21
16				35.0315	125.8022	05	48
17	2013	10	23	35.1479	125.8511	00	20
18				35.1497	125.8528	01	25
19				35.1826	125.8072	01	58
20				35.1465	125.8483	02	27
21				35.1830	125.8476	02	52
22				35.1477	125.8503	03	22
23				35.1442	125.8495	04	27
24				35.1811	125.8887	04	52
25				35.1425	125.8474	06	23
26				35.1061	125.8036	06	53

2.3. Aerosol Estimation Process for Turbid Waters

To analyze the effect of the stray light in the course of atmospheric correction, it is necessary to observe how the radiometric artefact propagates during the aerosol estimation process which is typically initiated in turbid waters. The iterative process of aerosol estimation embedded in the GDPS 1.3 atmospheric correction [9,11], is described briefly in the following.

(Step 1) Estimating aerosol reflectance in the NIR bands (745 and 865 nm)

Under a given reflectance budget of Rayleigh-corrected reflectance (ρ_a), the aerosol reflectance is obtained by subtracting $t\rho_w$ from ρ_{rc} as in

$$\rho_a (NIR) \leftarrow \rho_{rc} (NIR) - t\rho_w (NIR) \quad (9)$$

The water reflectance in the NIR bands is assumed zero at the first iteration; however, it will have non-zero values for turbid water as the iteration progresses.

$$\rho_w (NIR) = 0 \text{ (at the first iteration)} \quad (10)$$

(Step 2) Selecting the aerosol models and estimating aerosol reflectance

Based on the multiple-scattering ε , defined as

$$\varepsilon = \frac{\rho_a (745)}{\rho_a (865)} \quad (11)$$

the most probable aerosol models and their weightings are computed using the look-up table that relates multiple-scattering ε with single-scattering ε .

(Step 3) Updating $t\rho_w$ for the visible bands

Now that the aerosol reflectances for the visible bands ($\rho_a (VIS)$) are available, following Step 2, the water reflectance at 660 nm is updated as in

$$t\rho_w (660) \leftarrow \rho_{rc} (660) - \rho_a (660) \quad (12)$$

(Step 4) Estimating water reflectance at the NIR bands

According to the water reflectance model in the NIR wavelength region [12], the ρ_w of the NIR bands have a monotonic relationship with $\rho_w(660)$ formulated by a fourth-order polynomial.

$$\rho_w(745), \rho_w(865) = f(\rho_w(660)) \quad (13)$$

The water reflectances of the NIR bands are determined based on Equation (13).

(Step 5) Repeating Steps 1 through 4 until convergence

In the process, Steps 1 through 4 are repeated until ρ_a and ρ_w at a certain run have no significant changes compared with the previous iteration.

3. Results

As briefly mentioned in Introduction, CIDUM results are assessed with two approaches: (1) boundary analysis; and (2) *in situ* analysis. In the boundary analysis (Section 3.1), remote sensing reflectance data near a slot boundary are compared between an original image and the CIDUM-corrected image, where the differences in the atmospheric correction results are quantified in terms of Rayleigh-corrected, aerosol, and remote sensing reflectance. In the *in situ* analysis (Section 3.2), the changes in the reflectance variables before and after the CIDUM algorithm are assessed using *in situ* radiometric measurements, which are available not only in the slot boundary area but also in remote areas from the boundary.

3.1. Boundary Analysis

Before analyzing the results in R_{rs} , the correction results in the TOA radiance (L1B) data are first shown in Figure 2. Figure 2 shows images of TOA radiance both before and after the CIDUM correction: Band 6 ($L_{TOA}(680)$) in Figure 2a and Band 8 ($L_{TOA}(865)$) in Figure 2b. The color scales of the figures are adjusted to the areas of the ocean that are relatively clear, which makes high-reflectance targets such as clouds, high concentrations of aerosols, land areas, and ocean areas of high turbidity have saturated values (white). In both spectral bands, the discontinuity across the slot boundary between Slot 7 (upper slot) and Slot 10 (lower slot) is shown mitigated in the corrected images (right), recovering the continuity of the natural variability. Note that a certain amount of discontinuity is unavoidable because of the difference in acquisition time between the upper and lower slots (the difference in acquisition time between Slots 7 and 10 is around 5 min). To assess the improvement achieved by the correction, the ISRD is measured in terms of the relative mean difference (ψ) of the Rayleigh-corrected reflectance (ρ_{rc}) between the pixels in the slot overlaps:

$$\psi_{\rho_{rc}} = \sum_i^N \frac{\rho_{rc}^{(upper\ slot)} - \rho_{rc}^{(lower\ slot)}}{\rho_{rc}^{(lower\ slot)}} \quad (14)$$

where N is the total number of samples in the slot overlap used to compute the statistics. While the slot boundary with no evident SLRI had a value of $\psi_{\rho_{rc}} < 5\%$, according to the previous observations, this slot pair has large values of $\psi_{\rho_{rc}}$ of 6.9%, 15.6%, and 17.5% for Bands 5, 6, and 8, which were reduced to 2.4%, 4.9%, and 5.2%, respectively, after the correction.

Figure 3 shows the image of R_{rs} for Band 6 together with the R_{rs} profile along transect PQ. In the figure, high-reflectance targets that are ineligible for the regular atmospheric correction algorithm (e.g., land and cloud) are filled with the lowest values of the color scale and excluded from the analysis. In the R_{rs} image (Figure 3a), the effect of SLRI is clear in the upper slot (Slot 7) before the correction (left-hand figure), which induces overestimation in $R_{rs}(660)$ in the upper slot and significant discontinuity at the slot boundary. The R_{rs} profile along the vertical transect between points P and Q reveals that the discontinuity at the boundary point is due to overestimation. The correction removes

the overestimation from R_{rs} in the upper slot (right-hand figure), while maintaining the original local variability in the profile. The R_{rs} bias is largest at the bottom of the slot and it tapers off further north.

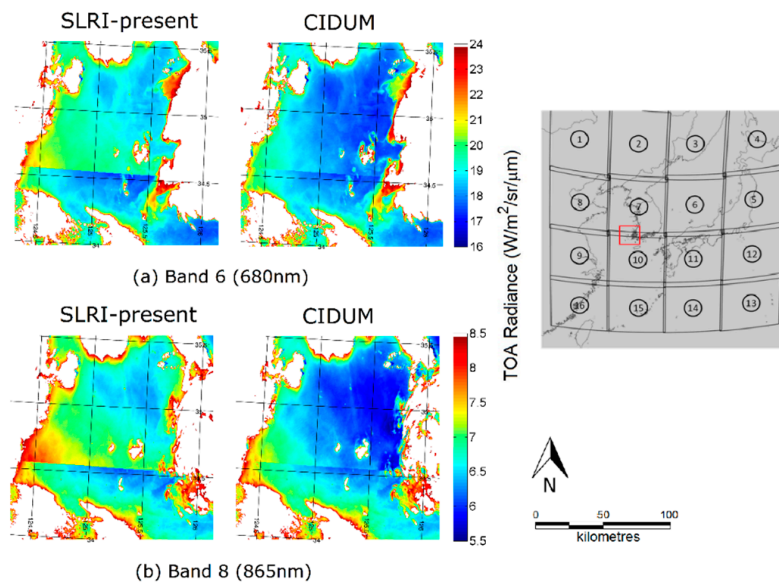


Figure 2. Images of GOCI TOA radiance acquired on October 16, 2012 (UTC 04): (a) Band 6; and (b) Band 8, both before and after the CIDUM correction. The location of the image area is marked in the slot area image of GOCI L1B data on the right.

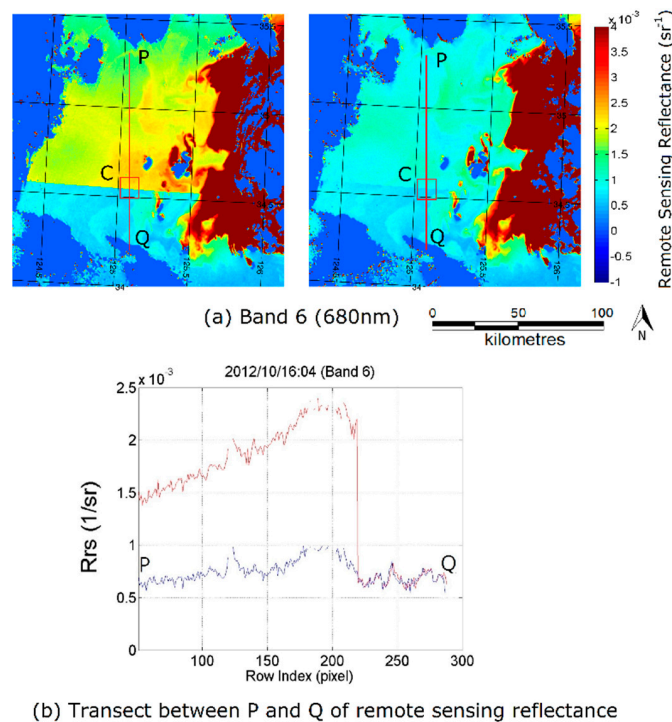


Figure 3. (a) Images of GOCI remote sensing reflectance acquired on 16 October 2012 (UTC 04) for Band 6 both before and after the CIDUM correction; (b) Profile of remote sensing reflectance along transect PQ.

To further investigate the impact on the atmospheric correction process, reflectance spectra of the intermediate products are plotted for the pixels in a small area (Box C) at the slot boundary.

The atmospheric correction process removes the reflectance contributed by Rayleigh scattering and aerosol scattering from the TOA reflectance measured at the sensor. TOA reflectance is expressed as

$$\rho_{TOA} = \rho_r + \rho_a + t_u \rho_w \quad (15)$$

$$\rho_{rc} = \rho_a + t_u \rho_w \quad (16)$$

where ρ_a is aerosol reflectance, ρ_w is water reflectance, and t_u is upward diffuse transmittance. The water reflectance is related to ρ_{rs} through

$$\rho_w = f t_d R_{rs} / \pi \quad (17)$$

where f is the coefficient for the bidirectional effect, and t_d is downward diffuse transmittance. We can obtain R_{rs} from ρ_{TOA} through the atmospheric correction. The effect of CIDUM can be assessed in terms of the three intermediate reflectance products in the process: the Rayleigh-corrected reflectance (ρ_{rc}), aerosol reflectance (ρ_a), and remote sensing reflectance (R_{rs}). Figure 4 presents the mean spectra of the three types of reflectance for the pixels of box C in Figure 3. For each type of reflectance, three different data sources were used: (1) pixels in the box that belong to the upper slot before the CIDUM correction (ρ^{SLRI}) (red line); (2) the same pixels as (1) but with SLRI corrected by CIDUM (ρ^{Corr}) (blue line); and (3) pixels in the box that belong to the lower slot (ρ^{Ref}) (green line). As mentioned earlier, because the uppermost part of the lower slot was assumed to have no SLRI, the statistics obtained from the lower slot pixels can be considered references under the assumption that the optical environment (e.g., aerosol loading and concentration of water constituents) does not vary significantly across the slots.

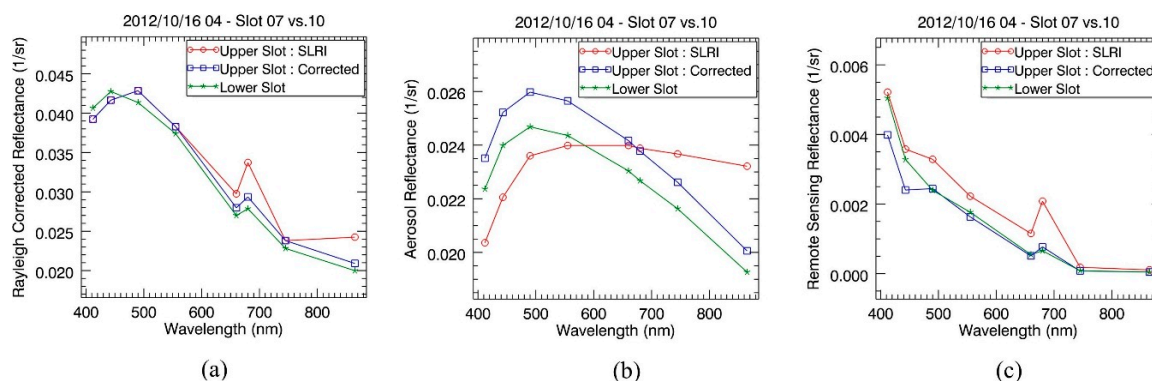


Figure 4. Spectra for (a) Rayleigh-corrected reflectance (ρ_{rc}); (b) aerosol reflectance (ρ_a); and (c) remote sensing reflectance for three types of data source (R_{rs}): (red) SLRI-present data, (blue) data corrected by CIDUM, and (green) reference data from the lower slot.

The ρ_{rc} spectra (Figure 4a) show that ρ_{rc}^{SLRI} is overestimated compared with ρ_{rc}^{Corr} with a relative difference of 4.8%, 18.1%, and 17.3% for Bands 5, 6, and 8, respectively. The large overestimation in Band 8 (865 nm) is critical in deriving R_{rs} , because the aerosol model and loading for the pixel location is estimated primarily based on the ρ_{rc} ratio of the two NIR bands (Bands 7 and 8), *i.e.*, the multiple scattering epsilon (ϵ). The values of ϵ before and after the correction are 3.4 and 6.5, respectively, which led to the significantly different aerosol reflectance spectrum over the GOCI spectral range, as shown in Figure 4b. The large ρ_{rc}^{SLRI} (865) values (which consequently led to low values of ϵ) caused ρ_a^{SLRI} (865) to be greatly overestimated and made ρ_a^{SLRI} of the visible bands (Bands 1–6) underestimated. Under the fixed total reflectance budget, the underestimation in ρ_a^{SLRI} in turn caused the overestimation of R_{rs}^{SLRI} in the corresponding spectral range, as shown in Figure 4c. CIDUM successfully corrected biases in all the three GOCI reflectance estimates induced by SLRI, producing GOCI remote sensing reflectance (R_{rs}^{Corr}) very close to that from the reference data (R_{rs}^{Ref}) (relative difference of <1% in all

bands except Band 1 and 2). The abrupt decreases in R_{rs} in the blue bands (Bands 1 and 2) that are unique in the samples in the upper slot are due to pixel response non-uniformity, where the detectors in the marginal area of the 2-dimensional detector array have non-uniform photo responsivity for Bands 1 and 2 [13]. The slight difference between the spectra of ρ_{rc}^{Corr} and ρ_{rc}^{Ref} which is considered to be induced by local variability in the aerosol condition was properly explained in the aerosol reflectance in Figure 4b, which then resulted in consistent remote sensing reflectance in ocean waters.

3.2. Assessment with in Situ Radiometric Measurements

In this section, the uncertainty of the GOCI R_{rs} is computed using the *in situ* R_{rs} measurements collected at the 26 stations near the slot boundary between Slots 7 and 10. For each *in situ* measurement, the temporally closest GOCI scene was selected and the average value of a 3×3 pixel window, centered at the *in situ* location, was compared with the *in situ* measurement. The maximum time difference between the GOCI and *in situ* data allowed in this validation was 1 h. Because of the high temporal resolution of GOCI (hourly from 09:00 to 16:00 local time), there are usually two GOCI scenes available for match-up. When multiple GOCI data were available for the match-up, the temporally closest GOCI data were used. A spatial homogeneity test was performed for the pixels in the window to verify whether the average values of the window were representative of the window area (the coefficient of variation was <5% in all the stations). Two statistics were used to evaluate the uncertainty in the resultant GOCI R_{rs} : the absolute mean percentage difference (APD, $|\psi_{Rrs}|$) and the relative mean percentage difference (RPD, ψ_{Rrs}), which are given as:

$$|\psi_{Rrs}| = \sum_i^N \left| \frac{R_{rs}^{(GOCI)} - R_{rs}^{(insitu)}}{R_{rs}^{(insitu)}} \right| \quad (18)$$

$$\psi_{Rrs} = \sum_i^N \frac{R_{rs}^{(GOCI)} - R_{rs}^{(insitu)}}{R_{rs}^{(insitu)}} \quad (19)$$

Figure 5a,b presents scatter plots of R_{rs} (555) between the GOCI and *in situ* data before and after the application of CIDUM, respectively. The overall data scatter (*i.e.*, $APD=|\psi_{Rrs}|$) was 16.1% before the correction, which was reduced to 11.1% after the correction, primarily because of the mitigated underestimation in the CIDUM-corrected data (Figure 5b), particularly for the R_{rs} range of 0.02–0.025. We defined the amount of correction (*Corr*) as

$$Corr = R_{rs}^{Corr} - R_{rs}^{SLRI} \quad (20)$$

and plotted the quantity ($R_{rs}^{in-situ} + Corr$) against the *in situ* R_{rs} in Figure 5c and d (*i.e.*, the small and large ranges of R_{rs} are shown in Figure 5c,d, respectively). While *Corr* is relatively small for stations with $R_{rs}(555) < 0.02$ (Figure 5c), larger corrections can be observed for stations with higher $R_{rs}(555)$, *i.e.*, samples from water with greater turbidity. In Figure 5d, most of the correction was positive for samples with $R_{rs}(555) > 0.02$ and it was greatest for the stations located closest to the slot boundary (*e.g.*, Stations 5–7, 9, 10 and 16). The mean suspended particulate matter (SPM) concentration of these six stations is above 40 g/m^3 , whereas the SPM of the stations in clear water is around 1 g/m^3 . The largest correction was made for Station 16 (SPM = 48.65 g/m^3), where *Corr* is ~ 0.006 , which accounts for $\sim 25\%$ of the corrected R_{rs} (R_{rs}^{Corr}).

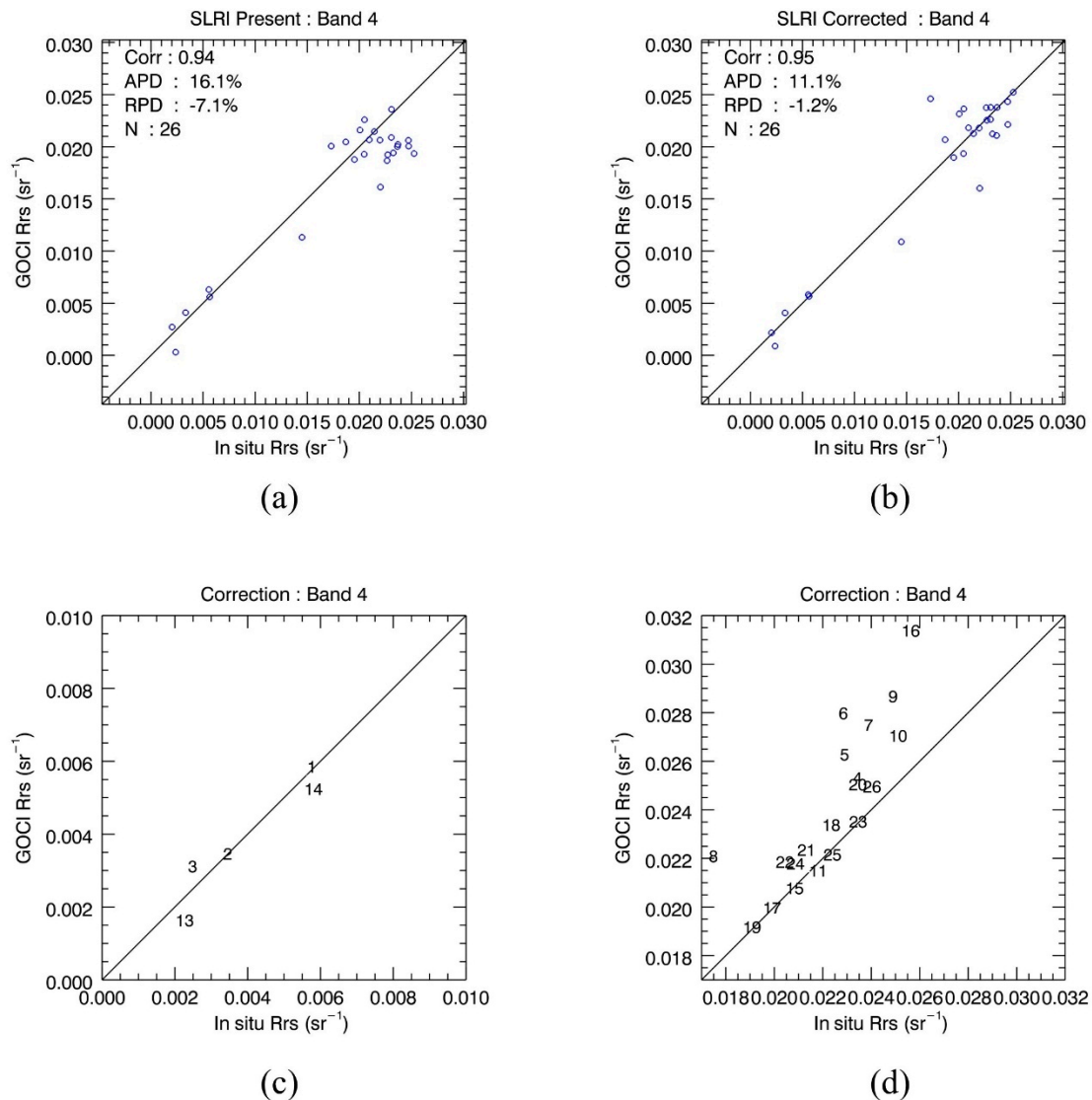


Figure 5. Scatter plots of remote sensing reflectance of Band 4 (R_{rs} (555)) between *in situ* and GOCI data: (a) before CIDUM and (b) after CIDUM. Changes in R_{rs} (*i.e.*, correction) are plotted on the one-to-one line with station ID's: (c) small R_{rs} values and (d) large R_{rs} values.

Spectrum analysis was performed for two stations selected from non-turbid and turbid waters: Station 14 was in relatively clear water ($SPM = 1.41 \text{ g/m}^3$) and Station 16 was in a turbid area ($SPM = 48.65 \text{ g/m}^3$). The Rayleigh-corrected reflectance (ρ_{rc}) spectra before and after the correction (Figure 6a,b) showed that the CIDUM effectively corrected the ρ_{rc} in the SLRI-affected bands. The *Corr* in Bands 5, 6, and 8 was 0.0020, 0.0048, and 0.0036 for Station 14 and 0.0031, 0.0070, and 0.0052 for Station 16. Note that the correction appears smaller in the figure for Station 16 because of the different scales of the y-axes. The relative corrections against the corrected ρ_{rc} values are 3.4%, 8.0%, and 16.2% for Station 14 and 8.0%, 19.5%, and 22.5% for Station 16 for Bands 5, 6, and 8, respectively.

Similar to the case in the previous boundary analysis, a large positive bias in ρ_{rc} (865) before the CIDUM correction induced an overestimation of the aerosol loading (*i.e.*, high ρ_a (865)) at the both stations. At Station 14, the smaller values of ε ($= \rho_{rc}(745)/\rho_{rc}(865)$) induced relatively flat aerosol reflectance over the entire wavelength range, which led to the underestimation of ρ_a in the visible bands. The underestimation of ρ_a induced an overestimation of R_{rs} , not only in the SLRI-affected bands but also in the other visible bands.

Contrary to the case of Station 14, the underestimated values of ϵ by SLRI for Station 16 led to greatly overestimated values of ρ_a across the entire spectral range (red curve in Figure 6d), which led to significant underestimation of R_{rs} across the entire range (red curve in Figure 6f). This opposite pattern stems from the complicated process of aerosol estimation that involves an iterative process for the separation of the aerosol and water reflectances from the Rayleigh-corrected reflectance. The discussion on the detailed mechanism is presented in Section 4.

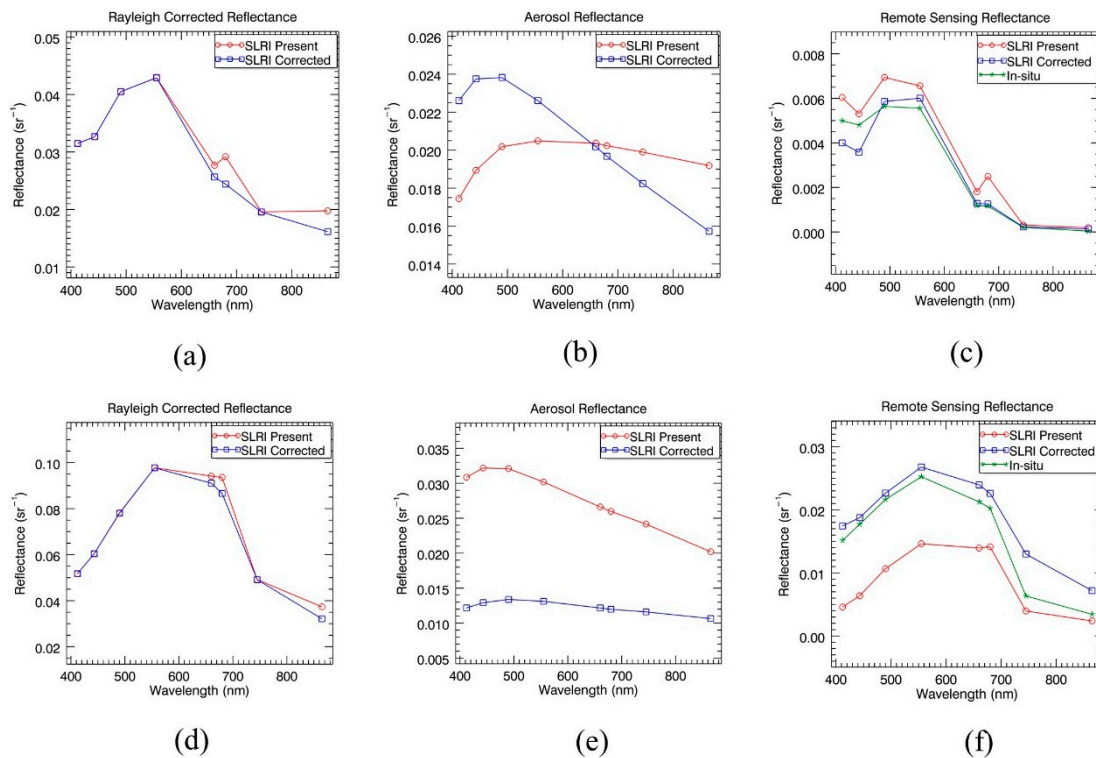


Figure 6. Spectra are presented for ((a) and (d)) Rayleigh-corrected reflectance (ρ_{rc}); ((b) and (e)) aerosol reflectance (ρ_a), and ((c) and (f)) remote sensing reflectance (R_{rs}). The upper row figures (a), (b), and (c) are for Station 14, and the bottom row figures (d), (e); and (f) are for Station 16. In each figure, reflectance curves for both SLRI-present data before CIDUM (red) and data corrected by CIDUM (blue) are presented. For remote sensing reflectance ((c) and (f)), reflectance spectra for *in situ* measurements (green) are presented additionally.

The resultant R_{rs} spectra show that the CIDUM correction generally mitigates both the overestimation and the underestimation caused by SLRI, making the GOCI R_{rs} much closer to the *in situ* R_{rs} . At Station 14, the overestimation of ρ_{rs} before the correction was 23%, 18%, 53%, and 113%, which was reduced to 4%, 8%, 8%, and 8% after the correction for Bands 3–6, respectively. The improvement was particularly significant for Band 6, which has a large impact on the estimation of the fluorescence signal from phytoplankton. The bias in the turbid water (Station 16) was -70% , -64% , -51% , -42% , -34% , and -30% before the correction, which was also greatly mitigated to 15%, 6%, 5%, 6%, 13%, and 12% for Bands 1–6, respectively.

The validation results for the other GOCI visible bands are presented in Table 2. Generally, the CIDUM improves the correlation between GOCI and *in situ* R_{rs} and it reduces data scatter. The improvement was largest in the blue bands, where the improvement in correlation was around 0.2 and the APD improvement was nearly 10% in the 412-nm band. The improvement in bias (RPD) is band-dependent, whereby the bias is generally reduced but some bands have poorer RPDs.

Table 2. Match-up validation results between *in situ* and GOCI data before and after the CIDUM correction for the six visible bands.

	Correlation		APD ($ \psi_{Rrs} $)		RPD (ψ_{Rrs})	
	Before	After	Before	After	Before	After
Band 1	0.55	0.74	40.4	29.7	−1.4	3.1
Band 2	0.79	0.87	30.0	22.9	−13.4	−13.8
Band 3	0.90	0.92	21.3	14.2	−7.7	−4.9
Band 4	0.94	0.95	16.1	11.1	−7.1	−1.2
Band 5	0.96	0.97	37.3	27.6	−22.3	−19.1
Band 6	0.96	0.96	35.4	24.4	−3.6	−12.8

4. Discussion

SLRI creates a positive bias in TOA radiance and consequently also in Rayleigh-corrected radiance/reflectance. However, in R_{rs} the bias is not necessarily positive because of the complicated process of aerosol estimation in the atmospheric correction as shown in our results. A question remains regarding the specific mechanism in the iterative process that decides the sign of the bias in R_{rs} . To analyze the mechanism, changes in the aerosol and water reflectances in the iterative process of aerosol estimation described in Section 2.3 were tracked over five iterations at the end of the iteration.

The iterative process is basically controlled by three constraints: (1) the total reflectance budget given by ρ_{rc} , as specified in Equation (15); (2) types of aerosol models and associated aerosol loadings, determined in Step 2 in Section 2.3; and (3) water reflectance relationship between the 660-, 745-, and 865-nm bands, as specified in Equation (13). The iterative process finds the combination of ρ_a and $t\rho_w$ that best fits the constraints under the reflectance budget of ρ_{rc} . Radiance data affected by SLRI will definitely produce different results from the case without SLRI in all or any of ρ_{rc} , ρ_a , and ρ_w . The aim here is to investigate how the radiance bias that is created by SLRI is propagated to the reflectance products in the process of aerosol estimation. Because the impact of SLRI in the NIR bands is most critical to the atmospheric correction process, we focused on tracking how the SLRI bias in the 865-nm band was resolved in the process, by comparing the reflectance values of the 865-nm band to the adjacent NIR band (745-nm band) that is free of SLRI. If we define the reflectance difference between the two NIR bands $\Delta\rho$ as

$$\Delta\rho = \rho(745) - \rho(865) \quad (21)$$

then three types of reflectance difference $\Delta\rho_{rc}$, $\Delta\rho_a$, and $\Delta t\rho_w$ can be defined accordingly for ρ_{rc} , ρ_a , and $t\rho_w$. The value $\Delta\rho_{rc}$ is always smaller in SLRI-affected data than in SLRI-corrected data, because SLRI (which is always positive) is present only in the 865-nm band and not in the 745-nm band. Figure 7 shows how the iterative process resolves the smaller $\Delta\rho_{rc}$ (solid red line) in the SLRI-affected data by changing $\Delta\rho_a$ and $\Delta t\rho_w$ over the five iterations. Our observations are focused on how the converged $\Delta\rho$'s (*i.e.*, values at the 5-th iteration in the figures) differ between the SLRI-affected and the SLRI-corrected data. At Station 14 (Figure 7a), when SLRI existed, it can be seen that the final values of $\Delta\rho_a$ and $\Delta t\rho_w$ are reduced in comparison with the values of $\Delta\rho_a$ and $\Delta t\rho_w$ in the SLRI-corrected data (blue). The reductions in $\Delta\rho_a$ and $\Delta t\rho_w$ are natural because the overall $\Delta\rho_{rc}$ budget is much tighter in the SLRI-affected data; thereby, the iterative process forced the values of $\Delta\rho_a$ and $\Delta t\rho_w$ to diminish to satisfy the reduced budget. Conversely, at Station 16 (Figure 7b), it can be seen that despite the smaller $\Delta\rho_{rc}$ budget in the SLRI-affected data, the value of $\Delta\rho_a$ increased. Figure 7b shows that even if the value of $\Delta\rho_a$ increases, the quantity of $\Delta\rho_a + \Delta t\rho_w$ is able to meet the reduced $\Delta\rho_{rc}$ budget because of the sufficiently large decrease in $\Delta t\rho_w$.

A question then arises regarding what is responsible for this difference in the mechanism resolving the SLRI in the 865-nm band between clear and turbid waters. The suggested explanation is that water reflectance in turbid waters (Station 16) has much greater flexibility in the water reflectance constraint specified in Equation (13) than in clear waters (Station 14). In turbid waters, water reflectance

in the red and NIR bands might have much larger values because of the high scattering by the suspended sediments, whereas clear waters have near-zero reflectance for the wavelength longer than 700 nm because of increasing water absorption. To resolve both the SLRI in the 865-nm band and the corresponding smaller $\Delta\rho_{rc}$, in the case of turbid waters, the aerosol estimation process changes the estimated turbidity and correspondingly, the $\Delta t\rho_w$, which leads to erroneous water reflectance. However, in the case of clear waters, there are no such water constituents to affect the optical properties in the red and NIR wavelengths (neither phytoplankton pigments nor dissolved organic matter play an important role in this wavelength region), which prohibits the aerosol-estimation process from altering the water reflectance to resolve the artifact caused by SLRI.

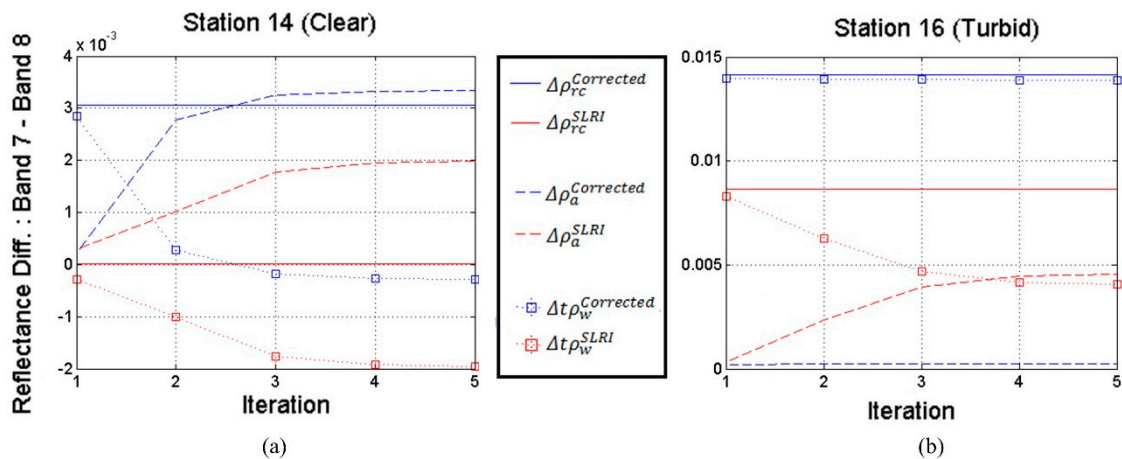


Figure 7. Changes in $\Delta\rho_{rc}$, $\Delta\rho_a$, and $\Delta t\rho_w$ over the final five iterations in the aerosol estimation process for (a) Station 14; and (b) Station 16.

Errors due to radiometric artefacts do not disappear in the iterative scheme unless the artefact is removed prior to the atmospheric correction. The errors oscillate between the atmospheric reflectance and water reflectance, and end up being more in one type of reflectance than in the other depending on the factors such as magnitude of artefact, aerosol types, and water types. It is highly likely that this is the case for other ocean color satellites [14,15], because they adopt a similar iterative approach for atmospheric correction in turbid waters. A major difference is that a biogenic optical model is used in the satellites for regulating the inter-band water reflectance rather than polynomial relationships as in GOCI's case. Atmospheric correction algorithms that assume inter-band relationship for aerosol reflectance [16,17] also seem vulnerable to this type of radiometric artefact that has band-specific effects. While the regulation of the shape of aerosol reflectance makes the estimation of aerosol reflectance less sensitive to the band-specific artefact, the effect of the artefact would be then more salient in the estimated water reflectance.

5. Conclusions

In this study, we validated the results of the correction of the interslot discrepancy using the minimum noise fraction transform (CIDUM) algorithm for Geostationary Ocean Color Imager remote sensing reflectance (R_{rs}) data using both image analysis and *in situ* radiometric measurements collected around the Korean Peninsula. For the test scene, CIDUM mitigated the interslot radiometric discontinuity by reducing the relative bias measured in terms of the Rayleigh-corrected reflectance to <5% in the stray-light-driven radiometric inflation (SLRI)-affected bands (660, 680, and 865 nm), and it also recovered the natural variability of remote sensing reflectance in the slot boundary area. The validation, performed with the 26 *in situ* radiometric measurements, showed that CIDUM improved R_{rs} accuracy in the visible bands, producing lower absolute mean percentage differences (by up to 10%) and higher correlations (by up to 0.2).

Contrary to the intuitive belief that the effect of SLRI would be less significant in turbid water, because the proportion of the SLRI of the total radiance is smaller in turbid water than in clear water, the impact of SLRI was larger for R_{rs} in turbid water, inducing significant underestimation in the visible bands. In both clear and turbid waters, SLRI in the 865-nm band induced inflated aerosol reflectance, but the repercussions in other spectral bands differed depending on turbidity. At the station in relatively clear water, SLRI induced a lower aerosol reflectance slope ($\rho_a(745) / \rho_a(865)$), and consequently, an underestimation of aerosol reflectance and an overestimation of remote sensing reflectance (R_{rs}) in the visible bands. In turbid water, the lower slope in the Rayleigh-corrected reflectance ($\rho_{rc}(745) / \rho_{rc}(865)$) induced by SLRI was mostly accounted for by the change in remote sensing reflectance, which led to significant underestimation of the remote sensing reflectance in the visible bands. Analysis of the aerosol estimation process suggested that the reason for the different responses to SLRI in clear and turbid waters was that SLRI is resolved primarily by falsely adjusting the estimated turbidity in the case of turbid waters, whereas in the case of clear waters, it primarily relies on adjusting the aerosol reflectance because of the lack of room for alteration in water reflectance as there are not sufficient optically active constituents in the red and NIR wavelengths in clear waters. As a result, the errors attributable to SLRI are greater in turbid waters because of the high flexibility in water reflectance models in the red and near-infrared (NIR) wavelength regions.

Future work will include the enhancement of the CIDUM algorithm for terrestrial areas. Currently, CIDUM is intended for ocean areas only, so all validation work has been performed for top-of-atmosphere radiance and remote sensing reflectance over such areas. As shown in the analysis in this study, the impact of SLRI is not necessarily smaller in high-radiance areas. The impact of SLRI and the improvement by the CIDUM algorithm should also be assessed with respect to the atmospheric correction algorithm for terrestrial areas.

Acknowledgments: This study was supported by the research awards titled “Application research for geostationary ocean satellite (2nd phase)” and “Development of the integrated data processing system for GOCI-II” granted by the Korea Ministry of Oceans and Fisheries. The authors appreciate the efforts from the GOCI operation team in KIOST (Hee-Jeong Han, Sun-Ju Lee, and Suk Yoon) in terms of raw data processing and data collection of GOCI data.

Author Contributions: Wonkook Kim wrote the paper, implemented the modified algorithm, designed/performed most of the experiments, and produced/analyzed the results. Jeong-Eon Moon led all the field campaigns and collected/processed/tabulated the *in situ* measurements used in the paper. Jae-Hyun Ahn ran the atmospheric correction algorithm, produced related data, and helped analyze the results of the atmospheric correction. Young-Je Park, as the PI of the associated projects, conceived the experiments and provided expert knowledge on the *in situ* data processing and the analysis of the results.

Conflicts of Interest: The authors declare no conflict of interest.

Abbreviations

The following abbreviations are used in this manuscript:

ISRD:	Interslot radiometric discrepancy
SLRI:	Stray-light-driven radiometric inflation
CIDUM:	Correction of the interslot discrepancy using the minimum noise fraction transform
GOCI:	Geostationary ocean color imager
MNF:	Minimum noise fraction
TOA:	Top of atmosphere
L1A:	Level 1A
L1B:	Level 1B
APD:	Absolute mean percentage difference
RPD:	Relative mean percentage difference
SPM:	Suspended particulate matter

Appendix: The Minimum Noise Fraction (MNF) Transform

The MNF transform is composed of a series of linear transforms. Input signal (L_i) is defined as the sum of signal and noise which are mutually uncorrelated for i -th pixel as in

$$L_i = S_i + N_i \quad (\text{A1})$$

where S_i and N_i are the signal and noise for the pixel. The first transform performs noise whitening of the input data (L_i) using a noise statistics derived from the noise component (N_i). The noise covariance matrix (C_N) is decomposed through eigen-decomposition as in

$$C_N = V_N \Lambda_N V_N^T \quad (\text{A2})$$

$$W_N = V \Lambda_N^{-\frac{1}{2}} \quad (\text{A3})$$

$$W_N^T C_N W_N = I \quad (\text{A4})$$

where V_N and Λ_N are the eigenvector and the eigenvalue matrix, respectively. Multiplication of $\Lambda_N^{-\frac{1}{2}}$ to the eigenvalue matrix (V) leads to the noise-whitening matrix (W_N), which makes the noise covariance matrix into the identity matrix as in Equation (A4). The noise-whitening process uncorrelates the noises present in the input data, and normalizes the magnitude of the uncorrelated noises into ones, allowing the noise-whitened data interpreted as the signal-to-noise ratio of the input data.

The covariance matrix of the noise-whitened data (\widehat{C}_L) is computed as

$$\widehat{C}_L = W_N^T C_L W_N \quad (\text{A5})$$

and the second eigen-decomposition is applied to the matrix as

$$V_L^T \widehat{C}_L V_L = \Lambda_L \quad (\text{A6})$$

where V_L and Λ_L are the eigenvector and the eigenvalue matrix of the noise-whitened covariance matrix \widehat{C}_L . The final MNF transform is the multiplication of the two eigenvector matrices as

$$T_{MNF} = V_L^T W_N^T \quad (\text{A7})$$

and the transformed data are expressed as

$$X_{MNF,i} = T_{MNF} L_i \quad (\text{A8})$$

References

1. Ryu, J.-H.; Han, H.-J.; Cho, S.; Park, Y.-J.; Ahn, Y.-H. Overview of Geostationary Ocean Color Imager (GOCI) and GOCI Data Processing System (GDPS). *Ocean Sci. J.* **2012**, *47*, 223–233.
2. Choi, J.-K.; Park, Y.-J.; Ahn, J.-H.; Lim, H.-S.; Eom, J.; Ryu, J.-H. GOCI, the world's first geostationary ocean color observation satellite, for the monitoring of temporal variability in coastal water turbidity. *J. Geophys. Res.* **2012**, *117*. [[CrossRef](#)]
3. Kang, G.; Coste, P.; Youn, H.; Faure, F.; Choi, S. An in-orbit radiometric calibration method of the geostationary ocean color imager. *IEEE Trans. Geosci. Remote Sens.* **2010**, *48*, 4322–4328. [[CrossRef](#)]
4. Kim, W.; Ahn, J.-H.; Park, Y.-J. Correction of stray-light-driven interslot radiometric discrepancy (ISRd) present in radiometric products of Geostationary Ocean Color Imager (GOCI). *IEEE Trans. Geosci. Remote Sens.* **2015**, *53*, 5458–5472.
5. Oh, E.; Hong, J.; Kim, S.-W. Novel ray tracing method for stray light suppression from ocean remote sensing measurements. *Opt. Express* **2016**, in press.

6. Green, A.A.; Berman, M.; Switzer, P.; Craig, M. A transformation for ordering multispectral data in terms of image quality with implications for noise removal. *IEEE Trans. Geosci. Remote Sens.* **1988**, *26*, 65–74. [[CrossRef](#)]
7. Goodenough, D.G.; Dyk, A.; Niemann, O.; Pearlman, J.S.; Chen, H.; Han, T.; Murdoch, M.; West, C. Processing Hyperion and ALI for forest classification. *IEEE Trans. Geosci. Remote Sens.* **2003**, *41*, 1321–1331. [[CrossRef](#)]
8. Vermote, E.F.; Tanre, D.; Deuze, J.L.; Herman, M.; Morcrette, J.J. Second simulation of the satellite signal in the solar spectrum, 6S: An overview. *IEEE Trans. Geosci. Remote Sens.* **1997**, *35*, 675–686. [[CrossRef](#)]
9. Moon, J.-E.; Park, Y.-J.; Ryu, J.-H.; Choi, J.-K.; Ahn, J.-H.; Min, J.-E.; Ahn, Y.-H. Initial validation of GOCI water products against *in situ* data collected around Korean peninsula for 2010–2011. *Ocean Sci. J.* **2012**, *47*, 261–277. [[CrossRef](#)]
10. Ahn, J.-H.; Park, Y.-J.; Kim, W.; Lee, B.; Oh, L.-S. Vicarious calibration of the Geostationary Ocean Color Imager. *Opt. Express* **2015**, *23*, 23236–23258. [[CrossRef](#)] [[PubMed](#)]
11. Gordon, H.; Wang, M. Retrieval of water-leaving radiance and aerosol optical thickness over the oceans with SeaWiFS: A preliminary algorithm. *Appl. Opt.* **1994**, *33*, 443–452. [[CrossRef](#)] [[PubMed](#)]
12. Ruddick, K.; Cauwer, V.D.; Park, Y.-H.; Moore, G. Seaborne measurements of near infrared water-leaving reflectance: The similarity spectrum for turbid waters. *Limnol. Oceanogr.* **2006**, *51*, 1167–1179. [[CrossRef](#)]
13. GOCI Sensor Calibration Team; (Korea Ocean Satellite Center, Korea Institute of Ocean Science and Technology, Ansan-si, Gyeonggi-do, Republic of Korea). Personal Communication, 2015.
14. Bailey, S.W.; Franz, B.A.; Werdell, P.J. Estimation of near-infrared water-leaving reflectance for satellite ocean color data processing. *Opt. Express* **2010**, *18*, 7521–7527. [[CrossRef](#)] [[PubMed](#)]
15. Shi, W.; Jiang, L.; Wang, M. Atmospheric correction using near-infrared bands for satellite ocean color data processing in the turbid western Pacific region. *Opt. Express* **2012**, *20*. [[CrossRef](#)]
16. Singh, R.K.; Shanmugam, P. Corrigendum to “A novel method for estimation of aerosol radiance and its extrapolation in the atmospheric correction of satellite data over optically complex oceanic waters” [*Remote Sensing of Environment* 142 (2014) 188–206]. *Remote Sens. Environ.* **2014**, *148*, 222–223. [[CrossRef](#)]
17. Saulquin, B.; Fablet, R.; Bourg, L.; Mercier, G.; d’Andon, O.F. MEETC2: Ocean color atmospheric corrections in coastal complex waters using a Bayesian latent class model and potential for the incoming sentinel 3—OLCI mission. *Remote Sens. Environ.* **2016**, *172*, 39–49. [[CrossRef](#)]



© 2016 by the authors; licensee MDPI, Basel, Switzerland. This article is an open access article distributed under the terms and conditions of the Creative Commons Attribution (CC-BY) license (<http://creativecommons.org/licenses/by/4.0/>).